

A Single-Stage Synchronized Switch Interface Circuit for Power Enhancement and Voltage Regulation in Electromagnetic Energy Harvesting

Jiacong Qiu ¹, Graduate Student Member, IEEE, Haoyu Wang ², Senior Member, IEEE, Minfan Fu ³, Senior Member, IEEE, and Junrui Liang ⁴, Senior Member, IEEE

Abstract—Synchronized switch interface circuits demonstrate good performance for electromagnetic energy harvesting applications, but lack adaptability in terms of harvested power. This article introduces an additional control degree of freedom by proposing two power control methods and implementing them in a synchronous current inversion and energy extraction (SCIEE) circuit. Theoretical analysis indicates that the single-stage system achieves higher efficiency for approximately 41.3% of the supported load range compared to using a commercial dc–dc regulator. In the load transient experiments, the proposed system maintains the output voltage well-regulated, with undershoot and overshoot below 0.2 V. The output voltage ripple is 0.15 V at an 18 mA load current. The proposed system is compared to three other options: a direct ac–dc harvesting circuit, the synchronous switch energy extraction (SSEE) circuit, and a two-stage harvesting system using a commercial dc–dc regulator and an open-loop SCIEE circuit. The proposed system supports a maximum load current of 29.47 mA, the highest among these options. In a field test, the proposed system supports successful integrated circuit long range (LoRa) packet transmissions and exhibits a broader supported load range than the SSEE or direct ac–dc harvest scheme.

Index Terms—Energy harvesting, synchronous switch interface circuit, voltage regulation.

I. INTRODUCTION

THE Internet of Things (IoT) technology has grown rapidly over the last few decades. As the number of deployed devices increases, powering those embedded devices has become increasingly expensive. On the other hand, energy is widely available in the ambient environment. Harvesting ambient energy to power the embedded devices in different applications, such as environmental monitoring [1], automotive systems [2],

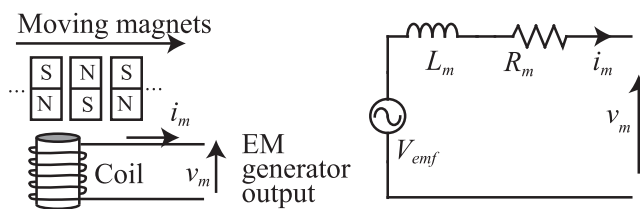


Fig. 1. General representation and circuit equivalent of an EMEH.

and smart home systems [3]. Ambient energy harvesting helps reduce the need for battery maintenance, leading to battery-free systems and lower costs.

Energy harvesters can convert ambient energy into electricity. Electromagnetic energy harvesters (EMEHs) are one of the most commonly used transducers [4]. EMEH has a decent power density and relatively lower output impedance [4]. Fig. 1 shows the schematic and circuit equivalent of an EMEH. V_{emf} represents the electromotive force (voltage). L_m and R_m are the coil's equivalent series inductance and resistance, respectively. This circuit equivalent is widely used in research on interface circuits for EM transducers [5], [6].

Different mechanical designs of EMEH have been proposed to harvest ambient energy. Those designs include cantilever beams or mass–spring systems to create translational movement between magnets and coils, thereby harvesting vibrational energy [6], [7], [8]. Such systems are suitable for vibration energy harvesting. The system modeling process in such EMEH usually involves considering the influence of electromagnetic damping introduced by interface circuits. On the other hand, EMEH designs have been proposed to harvest other types of kinetic energy as well. Rotational harvesters, similar to a generator, are suitable for harvesting energy from bicycles and other rotational movements. Some rotational EMEHs have also been proposed [9], [10], [11]. Slow but strong translational movements, such as tidal waves or human footsteps, can be converted into high-frequency rotational movements for better harvesting capability [12], [13]. When the mechanical input is strong, and the EMEH design can directly convert mechanical input to relative movement between magnets and coils, such as in [13], [14], and [15], the EMEH

Received 29 May 2025; revised 5 August 2025 and 2 October 2025; accepted 8 November 2025. Date of publication 11 November 2025; date of current version 19 January 2026. This work was supported by the National Natural Science Foundation of China under Grant 62271319. Recommended for publication by Associate Editor J. Biela. (Corresponding author: Junrui Liang.)

The authors are with the School of Information Science and Technology, ShanghaiTech University, Shanghai 201210, China (e-mail: qiujc@shanghaitech.edu.cn; wanghy@shanghaitech.edu.cn; fumf@shanghaitech.edu.cn; lian gjr@shanghaitech.edu.cn).

Color versions of one or more figures in this article are available at <https://doi.org/10.1109/TPEL.2025.3631630>.

Digital Object Identifier 10.1109/TPEL.2025.3631630

can be modeled by the simplified model shown in Fig. 1 with the amplitude of V_{emf} being regarded as constant.

The output of an EMEH is usually a low-voltage ac source, which is not directly utilizable for IoT devices. Interface circuits can convert the generated electricity of EMEH into utilizable forms. The most straightforward circuit is a full-bridge rectifier (FBR) or a voltage multiplier. The harvesting capability of such rectifiers is limited, since the output voltage level of EMEH is typically comparable to the diode voltage drop. Some early works reported using a rectifier to rectify the ac output of EMEH, followed by a boost converter [16], [17]. Active rectification can reduce the dissipation on diode voltage drop and is often used in integrated solutions [18], [19].

Direct ac–dc converters come from classic pulsewidth modulation (PWM) converters. They can enhance harvesting capability, boost output voltage, and reduce the dissipation on diodes. They are also capable of regulating the output voltage by controlling the duty cycle of the PWM switching signal. Multiple publications have investigated this type of topology [6], [20], [21], [22]. Some studies treat the output impedance (L_m and R_m) of the EMEH as a single entity or ignore it, incorporating an external inductor in the circuit topology for voltage boosting [21], [22]. Others utilize the internal inductance of the EMEH as the inductor for this purpose. Direct ac-to-dc converters typically operate in discontinuous conduction mode (DCM), as it offers advantages, such as source-load isolation and zero-voltage switching [22].

The synchronized switch (SS) technique has been proposed for piezoelectric transducers in [23]. The SS technique can significantly improve the harvesting performance of piezoelectric transducers [23], [24]. This technique can also enhance the harvesting capability of the EM transducer. Sun et al. [7] proposed the first interface circuit for EMEH based on the SS technique, naming it the SMFE circuit. The SMFE circuit outputs more power than the FBR in their experiment. Xie et al. [25] proposed an improved and self-powered version named synchronous switch energy extraction (SSEE) for rotational EMEH. The SSEE circuit harvested roughly twice as much energy as FBR in their experiment. Another self-powered SMFE has been proposed in [15] and can harvest more power than a voltage doubler.

Some articles reported that harvesting energy from EMEH and piezoelectric transducers simultaneously is also feasible. Jia et al. [26] proposed using two self-powered interface circuits for EMEH and piezoelectric transducers, respectively, and merging the output energy flows with diodes. Lombardi and Lallart [27] reused the EMEH's coil inductance as the inductive element for the piezoelectric transducer's interface circuit to achieve simultaneous energy harvesting. The synchronous current inversion and energy extraction (SCIEE) circuit has been proposed for EMEH in [28]. SCIEE outperforms SSEE and direct ac–dc under a relatively high coil quality factor. Existing SS circuits for EMEHs operate on a fixed control scheme; the control signal's waveform or phase does not change during the operation process. The impact of introducing control delays into the control signal for SS-based energy harvesting systems, where the source impedance significantly influences system behavior, has not been explored in previous studies.

The ability to control the output power of the interface circuit is helpful in IoT applications. Most embedded devices require a stable dc voltage supply, typically in the range of 1.8–5 V, with 3.3 V being the most common. If the interface circuit directly powers an embedded device, then it should be able to output a regulated dc voltage [29]. Meanwhile, when the interface circuit charges an energy storage element, such as batteries, capacitors, or supercapacitors, it should be able to regulate the output power to maintain good charging efficiency and prevent the storage element from exceeding its voltage limit.

Direct ac–dc converters can control their power by tuning the duty cycle of their control signal. Numerous studies have reported that this ability enables functionalities, such as voltage regulation, maximum power point tracking, and torque control [6], [22], [29], [30].

Conventional direct ac–dc converters can output a regulated dc voltage to power IoT devices. However, the mismatch between the output power and the power requirements of the IoT devices remains significant in energy harvesting applications. So, conventional active rectifiers struggle to meet the power requirements of IoT devices. Alternatively, SS circuits are reported to exhibit higher output power for some EMEHs [7], [15], [25], [28]. Thus, using SS interface circuits to power IoT devices has potential for improved performance. However, SS interface circuits for EMEH reported in previous articles lack the control degree of freedom and cannot output a stable dc voltage for IoT devices to operate. This article proposes an SS energy harvesting circuit for EMEH featuring two power control methods: phase delay control and energy extraction (EE) interval control. The proposed method is implemented in the SCIEE circuit. The proposed method introduces an additional control degree of freedom for electromagnetic synchronized switch interface circuits, enabling load voltage regulation and thereby extending their potential in energy harvesting IoT applications.

II. OPERATION PRINCIPLE

A. Circuit Topology

Fig. 2 shows the circuit schematic and operation waveform of the SCIEE circuit with phase delay control. The operation waveform of the EE interval control method is shown in Fig. 4, both with an enlarged waveform on the right.

The SCIEE circuit comprises a sensing inductor, an inversion branch, and a harvesting branch. L_m and R_M are the internal impedance of the EMEH. L_s is the sensing inductor, whose inductance is much smaller than L_m . R_s is the equivalent series resistance (ESR) of L_s . The controller can sense the voltage zero-crossing points (ZCPs) across L_s and generate control signals for v_{g1} and v_{g2} accordingly [31]. L_h is the harvesting inductor, designed to be much larger than L_m . C_s is the output capacitor. R_L is the load represented by a resistor. The voltage across C_s can be considered constant. C_1 is for the energy transfer process during energy harvesting. C_1 is rather small so that the resonant frequency of C_1 and L_m is much higher than the frequency of V_{emf} . C_2 is for the current inversion (CI) process. For simplicity of design and analysis, we set $C_2 = C_1$, but they do not have to be equal for the circuit to function normally.

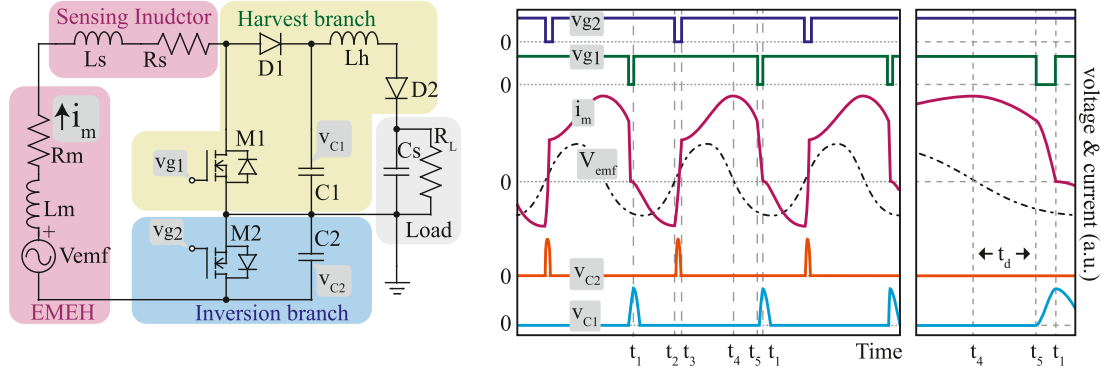


Fig. 2. Circuit schematic and operation waveform when control is realized by delaying the energy harvesting process by a certain amount. The delay time duration is t_d .

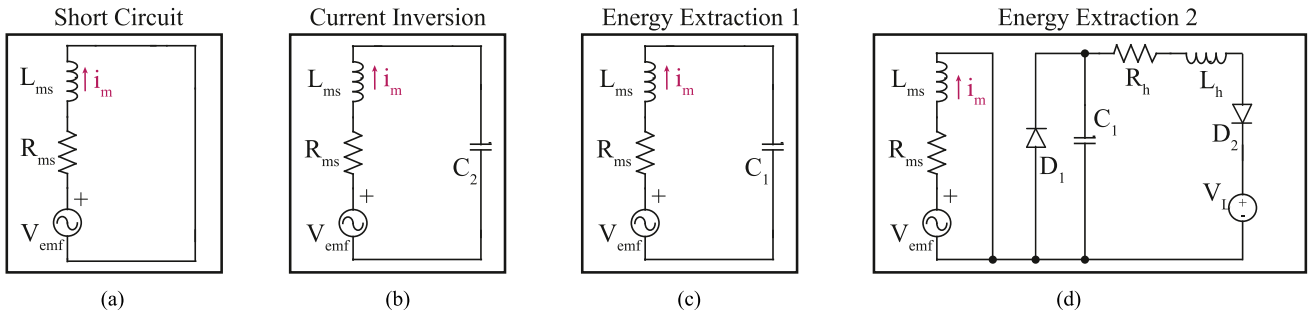


Fig. 3. Equivalent circuit diagrams. $L_{ms} = L_m + L_s$, $R_{ms} = R_m + R_s$. (a) SC mode. (b) CI mode. (c) EE 1 mode. (d) EE 2 mode.

B. Phase Delay Control

Fig. 2 shows the operation waveform when control is realized by delaying the energy harvesting phase.

At t_1 , the EMEH current $i_m = 0$. M_1 and M_2 are both ON to short-circuit (SC) the EMEH. The equivalent circuit is shown in Fig. 3(a). v_{emf} energizes L_m , and i_m rises between t_1 and t_2 . The harvested energy is stored inside L_m . This mode lasts until the first current peak of EMEH.

At t_2 , i_m reaches its negative peak. At this time, M_2 turns OFF, steering the current in EMEH to C_2 . L_m , L_s , and C_2 form an LC resonant loop; the equivalent circuit is in Fig. 3(b). The LC resonance lasts half a resonant cycle and inverts the EMEH current from negative to positive. When v_{C2} drops back to zero at t_3 , the body diode of M_2 conducts again to SC the EMEH. Turning M_2 ON after t_3 can reduce the conduction loss and realize zero-voltage switching for M_2 at t_3 .

After t_3 , the transducer is short-circuited with a nonzero initial current, as in Fig. 3(a). Energy accumulates in L_m , making i_m rise. Some initial current in the EMEH introduces more torque, so more energy is extracted from the mechanical domain than in the previous SC phase. At t_4 , i_m reaches its positive peak.

After t_4 , the circuit keeps the EMEH short-circuited until t_5 . t_d , the time delay between t_4 and t_5 , is tunable. Longer t_d results in less energy output and less torque induced in the EMEH, as the theoretical analysis in the next section shows. The controller can control the output power by controlling t_d . The minimum

energy output is achieved when i_m is negative at t_5 . In that case, turning OFF M_1 will have no effect since the EMEH will still be short-circuited by the body diode of M_1 .

At t_5 , the circuit starts to harvest energy. The amount of energy stored in the EMEH at t_5 determines the amount of extracted energy in this phase, as in Fig. 3(c). At t_5 , M_1 turns OFF to steer i_m through D_1 to C_1 . L_m and C_1 form a resonant loop to transfer the energy stored in the EMEH to C_1 . L_h is much larger than L_m , so it has a negligible impact on the LC resonance. This resonance lasts for a quarter of a resonant cycle of L_m and C_1 . When i_m reaches 0 at t_1 , D_1 becomes reverse biased. The EMEH is short-circuited with zero initial current to accumulate energy for the next cycle. In the meantime, the energy stored in C_1 transfers to the load through L_h and D_2 , as in Fig. 3(d).

The circuit operation suggests that the turn-OFF intervals of M_1 and M_2 do not need to be precise for the phase delay control method. If $t_d = 0$, then the circuit operates like a regular SCIEE circuit in [28].

C. EE Interval Control

Fig. 4 shows the operation waveform when controlling the length of the energy harvesting phase.

At t_1 , there is some initial current in the EMEH, $i_m > 0$. The EMEH is short-circuited by M_1 and M_2 until t_2 . Fig. 3(a) shows the equivalent circuit in this mode. Between t_1 and t_2 , $V_{emf} < 0$,

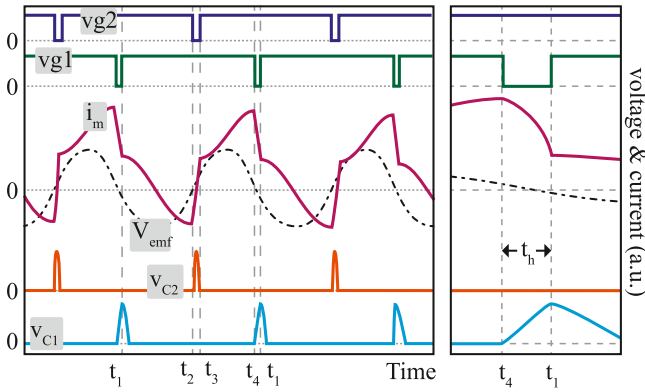


Fig. 4. Operation waveform of controlling the EE interval of the switch during the energy harvesting phase. t_h is the EE interval.

so i_m goes from positive to negative. This mode lasts until i_m reaches its negative peak at t_2 .

The circuit inverts the EMEH current between t_2 and t_3 , similar to the phase delay control method, and the equivalent circuit is in Fig. 3(b). In both cases, the CI occurs at the negative current peak of the EMEH. After the CI, the EMEH is again short-circuited until t_4 , the positive current peak.

At t_4 , M_1 turns OFF for t_h . When M_1 turns OFF, i_m is steered to the harvesting branch, similar to the phase delay control method, as in Fig. 3(c). However, for EE interval control, not all the energy stored in the EMEH is transferred to C_1 . At t_1 , M_1 turns ON again to SC the EMEH and make D_1 reverse-biased, as in Fig. 3(d). The circuit goes back to its initial state. On the other hand, the extracted energy in C_1 transfers to the load through D_2 and L_h . The amount of extracted energy in this mode is determined by the beginning and end values of i_m .

The EE interval t_h is tunable. Shorter t_h results in less energy output and less torque induced in the EMEH. The EE interval is the turn-OFF interval of M_1 . Therefore, for EE interval control, the turn-OFF interval of M_1 needs to be precise.

If $t_h \geq 0.5\pi\sqrt{(L_m + L_s)C_1}$, which is a quarter of the LC cycle of $L_m + L_s$, then the circuit operates like a regular SCIEE circuit.

Since the energy harvesting process of SCIEE and SSEE is similar, the same control method also applies to the SSEE circuit. Section V-D provides more details on using such control methods on the SSEE circuit.

III. THEORETICAL ANALYSIS

A. Output Energy of EMEH

The current level of EMEH, both before and after the EE phase, determines its energy output. Most of the extracted energy is transferred to C_1 and delivered to the load. To analyze the output energy of the EMEH, i_m at different time instances (e.g., t_1 and t_2) must be derived.

After obtaining the output energy, we can derive the energy delivered to the load by analyzing the energy flow of the harvest branch. Since the harvest branch consists of all switching elements and lossless elements, the energy output of the EMEH can

be fully transferred to load R_L given D_1 , L_h , D_2 , and C_1 are all ideal in steady state. For nonideal cases where L_h has ESR and diodes have voltage drops, a detailed analysis of the losses in the harvest branch is presented in [28]. Overall, the output energy of EMEH can reflect the energy delivered to the load side.

B. EMEH Model

In the following discussion, we assume that the electrical damping introduced by the interface circuit does not affect the dynamics of the EMEH. This assumption is suitable for applications where the EMEH design directly converts the mechanical input into the movement of magnets, as in [13], [14], and [15]. The EMEH's circuit equivalent is an ac voltage source with constant amplitude in series with a nonideal inductor, as shown in Fig. 1.

C. EMEH Energy Analysis of Phase Delay Control

Fig. 5(a) shows one cycle of the EMEH's current waveform when the control method is phase delay control, and Fig. 5(b) shows the waveform of EE interval control. The CI and EE phase is extended to illustrate the voltage waveform. Fig. 5(c) and (d) shows the equivalent circuits. We assume that the electromotive force (generated voltage) is a sinusoidal voltage

$$V_{emf} = V_0 \sin(\omega t) \quad (1)$$

where ω is the source angular velocity and V_0 is the amplitude. V_{emf} is also the open-circuit output voltage of the EMEH, so one can extract the parameters of V_{emf} by measuring the open-circuit output voltage of the EMEH.

The operation of phase delay control ensures that $i_m(t_1) = 0$. In the first SC phase, which is from t_1 to t_2 , the governing equation of the system is

$$-V_0 \sin(\omega t + \omega t_d) = L_{ms} \frac{di_m(t)}{dt} + R_{ms} i_m(t) \quad (2)$$

where t_d is the controllable delay time mentioned in Fig. 2, and $L_{ms} = L_m + L_s$, and $R_{ms} = R_m + R_s$ denote the inductance and resistance in the SC loop, respectively. Solving (2), I_{1d} , the current level at t_2 , is obtained as

$$i_m(t_2) = I_{1d}(t_d) = -\frac{\omega L_{ms} V_0}{X_{ms}} - \frac{V_0 e^{\frac{\omega t_d - \pi}{Q}}}{\sqrt{X_{ms}}} \sin(-\omega t_d + \phi) \quad (3)$$

where $X_{ms} = R_{ms}^2 + L_{ms}^2 \omega^2$, $Q = \omega L_{ms} / R_{ms}$ is the EMEH quality factor, and $\phi = \arctan(Q)$.

In the CI phase (t_2 to t_3), as shown in Fig. 5(d), an RLC resonant circuit resonates for half a resonance period. Then, the EMEH current at t_3 is

$$I_{2d}(t_d) = \gamma I_{1d}(t_d) \quad (4)$$

where $\gamma = -\exp(-\pi/2Q_e)$, $Q_e = \omega_e L_{ms} / R_{mse}$ is the quality factor during CI phase, R_{mse} is the ESR of the EMEH at the resonance frequency of L_{ms} and C_1 , which is usually higher than R_{ms} , and $\omega_e = (L_{ms} C_1)^{-1/2}$ is the resonant angular frequency of L_{ms} and C_1 .

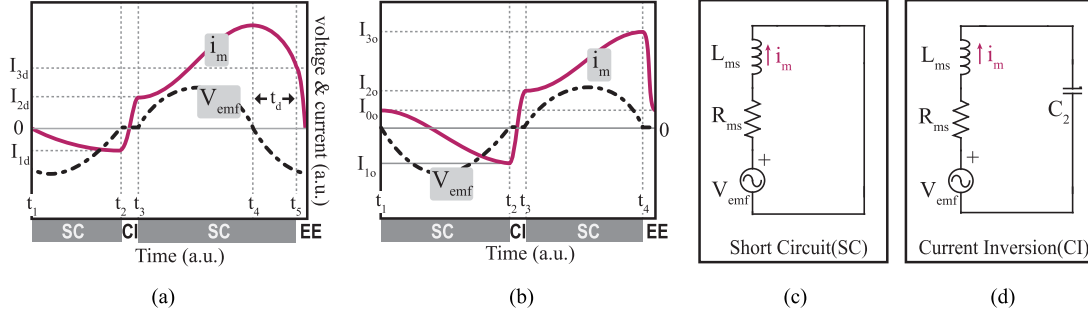


Fig. 5. Operation waveform of the EMEH current and simplified equivalent circuit during SC and CI. The impedance of EMEH and the sensing inductor are combined as $L_{ms} = L_m + L_s$ and $R_{ms} = R_m + R_s$. (a) EMEH voltage and current of phase delay control. (b) EMEH voltage and current of the EE interval control. (c) equivalent circuit during an SC. (d) equivalent circuit during CI.

In the next SC phase (t_3-t_5), the governing equation of the system is

$$V_0 \sin(\omega t) = L_{ms} \frac{di_m(t)}{dt} + R_{ms} i_m(t) \quad (5)$$

where the initial condition is changed as $i_m(0) = I_{2d}$. Solving (5), the value of the current level at t_5 is obtained as

$$I_{3d}(t_d) = e^{-(\omega t_d + \pi)/Q} \frac{(\gamma + 1)\omega L_{ms} V_0}{X_{ms}} + \frac{V_0(\gamma e^{-2\pi/Q} + 1)}{\sqrt{X_{ms}}} \sin(-\omega t_d + \phi). \quad (6)$$

Therefore, the energy output per cycle of the EMEH in phase delay control is

$$E_{PD}(t_d) = \frac{1}{2} L_{ms} (I_{3d}(t_d))^2. \quad (7)$$

So, the output power of the EMEH is

$$P_{PD}(t_d) = E_{PD}(t_d) \cdot \omega / 2\pi. \quad (8)$$

D. EMEH Energy Analysis of EE Interval Control

Fig. 5(b) shows one cycle of the EMEH's current waveform when the control method is EE interval control. At t_1 , the EMEH current is I_{0o} . From t_1 to t_2 , the governing equation is

$$-V_0 \sin(\omega t) = L_{ms} \frac{di_m(t)}{dt} + R_{ms} i_m(t) \quad (9)$$

and the initial condition is $i_m(0) = I_{0o}$. Solving (9) for I_{1o} gives

$$I_{1o} = e^{\frac{-\pi}{Q}} I_{0o} - I_x \quad (10)$$

which is the EMEH current at t_2 , and

$$I_x = (1 + e^{-\pi/Q}) L_{ms} \omega V_0 / X_{ms}. \quad (11)$$

I_x the current level of the EMEH if it is shorted for half a source cycle, with the initial current being zero and the phase of V_{emf} being also 0. It is also the peak current level of the SSEE circuit.

The circuit behaves like the phase delay control case in the CI phase, from t_2 to t_3 . The EMEH current is inverted from I_{1o} to I_{2o} , where

$$I_{2o} = \gamma I_{1o}. \quad (12)$$

In the next SC phase (t_3 to t_4), the governing equation is

$$V_0 \sin(\omega t) = L_{ms} \frac{di_m(t)}{dt} + R_{ms} i_m(t) \quad (13)$$

and the initial condition is $i_m(0) = I_{2o}$. This state is similar to (9), but the polarity of the initial current and V_{emf} are both positive in this phase. Solving (13) for I_{3o} gives

$$I_{3o} = e^{-\pi/Q} I_{2o} + I_x. \quad (14)$$

In the EE phase from t_4 to the next t_1 , the EMEH current drops from I_{3o} to I_{0o} . We define the ratio between I_{0o} and I_{3o} as $D_r(t_h)$, i.e.,

$$D_r(t_h) = I_{0o} / I_{3o}. \quad (15)$$

This ratio $D_r(t_h)$ is determined by the EE interval t_h if the output voltage level is lower than half of the peak voltage level on C_1 [28]. If the previously mentioned condition is not satisfied (usually under very light load), then $D_r(t_h)$ will be determined by the EE interval t_h , the average output voltage, and the average output current. However, D_r will still be dominated by t_h . The analysis of D_r is in Section III-E.

The value of I_{3o} and I_{0o} can be solved by combining (10), (12), and (14), which yields

$$I_{3o}(t_h) = \frac{(1 - \gamma e^{-\pi/Q})}{1 - \gamma \cdot D_r(t_h) \cdot e^{-2\pi/Q}} I_x \quad (16)$$

$$I_{0o}(t_h) = I_{3o} \cdot D_r(t_h). \quad (17)$$

By the conservation of energy, the energy output of the EMEH of the EE interval control is

$$E_{TO}(t_h) = \frac{1}{2} L_{ms} (I_{3o}(t_h))^2 - \frac{1}{2} L_{ms} (I_{0o}(t_h))^2. \quad (18)$$

Thus, the output power of the EMEH is

$$P_{TO}(t_h) = E_{TO}(t_h) \cdot \omega / 2\pi. \quad (19)$$

E. Relationship Between Harvest Time and Harvested Energy

The circuit in the EE phase is an LC resonant circuit with a diode in its current path, as discussed in the previous section. If the output voltage level is lower than half of the peak voltage level on C_1 , then the initial voltage on C_1 is 0, and the initial current in the inductor is I_{3o} . The current waveform of i_m

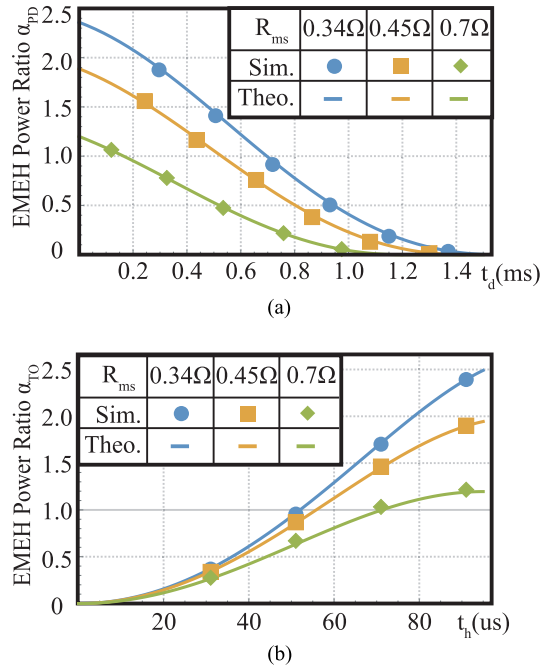


Fig. 6. Theoretically derived and simulated power of EMEH under: (a) phase delay control and (b) EE interval control.

during EE can be approximated as $i_m(t) \approx I_{3o} \cos(\omega_{e1}t)$, where $\omega_{e1} = (L_{ms}C_1)^{-1/2}$ is the resonant angular frequency of L_{ms} and C_1 . $D_{r-H}(t_h)$, D_r under relatively heavy load, is

$$D_{r-H}(t_h) = \cos(\omega_{e1} \cdot t_h). \quad (20)$$

If t_d is much shorter than the maximum duration of the EE phase, then $i_m(t)$ during the EE phase can be linearized. In this condition, the initial voltage on C_1 can be approximated as $V_{C0} \approx V_L$, where V_L is the output voltage. Then, $i_m(t) \approx I_{3o} - \frac{V_L}{L_{ms}}t$. $D_{r-VL}(t_h)$, D_r under very light load, is

$$D_{r-VL}(t_h) = 1 - \frac{V_L t_h}{L_{ms} I_{3o}}. \quad (21)$$

We define $\alpha_{PD} = P_{PD}/P_{opt}$ and $\alpha_{TO} = P_{TO}/P_{opt}$ as the EMEH power ratios. The power ratios indicate the output power. P_{opt} is the maximum power that can be delivered to a pure resistive load if it is directly connected to the output of the EMEH. P_{opt} is given by

$$P_{opt} = \frac{V_0^2 \sqrt{X_{ms}}}{2 \left(L_{ms}^2 \omega^2 + (R_{ms} + \sqrt{X_{ms}})^2 \right)}. \quad (22)$$

Fig. 6 shows the theoretically derived α_{PD} and α_{TO} , compared with the simulation results. The parameters are $V_0 = 1$ V, $L_{ms} = 1.6$ mH, $\omega = 211 \cdot 2\pi$ rad/s, $R_{mse} = R_{ms}$, and $R_L = 150$ Ω , other circuit elements are ideal.

To further validate the approximations made in the theoretical analysis, the simulated operation waveform under different control methods and different control signals is recorded and compared to theoretical values. Fig. 7 shows four cases. $R_{mse} = R_{ms} = 0.45$ Ω , other conditions are the same as the previous simulation. The simulated waveforms agree with the theoretical

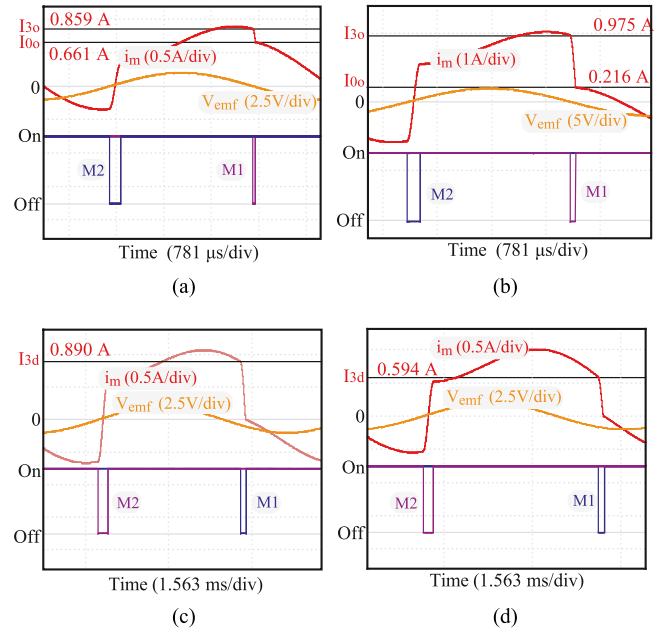


Fig. 7. Simulated operation waveform of: (a) EE interval control, $t_h = 40$ μ s. (b) EE interval control, $t_h = 80$ μ s. (c) Phase delay control, $t_d = 326$ μ s. (d) Phase delay control, $t_d = 737$ μ s.

TABLE I
CALCULATED AND SIMULATED CRITICAL CURRENT VALUES

Values	Simulation (A)	Theory (A)
$I_{3o} (t_h = 40 \mu\text{s})$	0.859	0.853
$I_{0o} (t_h = 40 \mu\text{s})$	0.661	0.665
$I_{3o} (t_h = 80 \mu\text{s})$	0.975	0.969
$I_{0o} (t_h = 80 \mu\text{s})$	0.216	0.213
$I_{3d} (t_d = 326 \mu\text{s})$	0.890	0.881
$I_{3d} (t_d = 737 \mu\text{s})$	0.594	0.589

analysis. Table I summarizes and compares the simulated values in Fig. 7(a)–(d) with theoretically calculated values using (6), (16), (17), and (20).

The two simulations show that simulated and theoretical values align well, validating the theoretical analysis on the EMEH currents and output power. Both control methods allow EMEH's output power to be adjusted from 0 to maximum.

F. Efficiency and Loss Analysis

The input energy from the mechanical domain is

$$E_{in} = \int_0^T V_{emf}(t) \cdot i_m(t) dt \quad (23)$$

and the energy loss on R_m and R_s are

$$E_{Loss_{ms}} = \int_0^T R_{ms} \cdot i_m^2(t) dt \quad (24)$$

where $T = 2\pi/\omega$ is the period of the EMEH voltage source, V_{emf} is given by (1), and $i_m(t)$ is given by solving (2), (5), (9), and (13).

1) *Current of Phase Delay Control*: Solving (2) gives the transducer current $i_m(t)$ in the first SC phase between t_1 and t_2

$$i_m(t) = \frac{V_0}{X_{ms}} \cdot [\omega L_{ms} \cos(\omega t + \omega t_d) - R_{ms} \sin(\omega t + \omega t_d)] + \frac{e^{-\omega t/Q} V_0}{X_{ms}} \cdot [R_{ms} \sin(\omega t_d) - \omega L_{ms} \cos(\omega t_d)]. \quad (25)$$

During CI phase, $i_m(t)$ is given by

$$i_m(t) = e^{-\omega_e(t_{ci})/Q} \cdot I_{1d} \text{Cos}(\omega_e t_{ci}) \quad (26)$$

where $t_{ci} = t + t_d - T/2$.

In the next SC phase, solving (5) gives $i_m(t)$ between t_3 and t_5 . Given the CI phase being much shorter than the EMEH period T , we have

$$i_m(t) = \frac{e^{-\omega t_{ci}/Q}}{X_{ms}} (I_{2-d} X_{ms} + L_{ms} V_0 \omega) + \frac{V_0}{X_{ms}} [-\omega L_{ms} \cos(\omega t_{ci}) + R_{ms} \sin(\omega t_{ci})]. \quad (27)$$

2) *Current of EE Interval Control*: For EE interval control, solving (9) gives the EMEH current between t_1 and t_2

$$i_m(t) = \frac{e^{-\omega t/Q}}{X_{ms}} (I_{0o} X_{ms} - L_{ms} V_0 \omega) - \frac{V_0}{X_{ms}} [-\omega L_{ms} \cos(\omega t) + R_{ms} \sin(\omega t)]. \quad (28)$$

During CI phase, $i_m(t)$ is given by

$$i_m(t) = e^{-\omega_e(t_{ci2})/Q} \cdot I_{1o} \text{Cos}(\omega_e t_{ci2}) \quad (29)$$

where $t_{ci2} = t - T/2$.

Similar to the first SC phase, the EMEH current between t_3 and t_4 can be approximated with

$$i_m(t) = \frac{e^{-\omega t_{ci2}/Q}}{X_{ms}} (I_{0o} X_{ms} + L_{ms} V_0 \omega) + \frac{V_0}{X_{ms}} [-\omega L_{ms} \cos(\omega t_{ci2}) + R_{ms} \sin(\omega t_{ci2})]. \quad (30)$$

Combining the equation of $i_m(t)$ and the currents of other components in the previous analysis, the input energy from the mechanical domain, the output energy at the load side, and the energy loss in one complete cycle can be theoretically derived. Fig. 8 shows the theoretically derived power and efficiency under different t_d , and Fig. 9 shows the results under different t_h . The amplitude of V_{emf} is 1.0 V, the ESR of L_h is 0.9 Ω , and the diode voltage drop is 1 V in the calculation. The results show that input power and output power both increase with the control signal, with the input power increasing faster at heavy load conditions. It also suggests that for EMEHs with a relatively low ESR, the EE interval control can maintain a relatively high efficiency across the load range compared to high-ESR EMEHs.

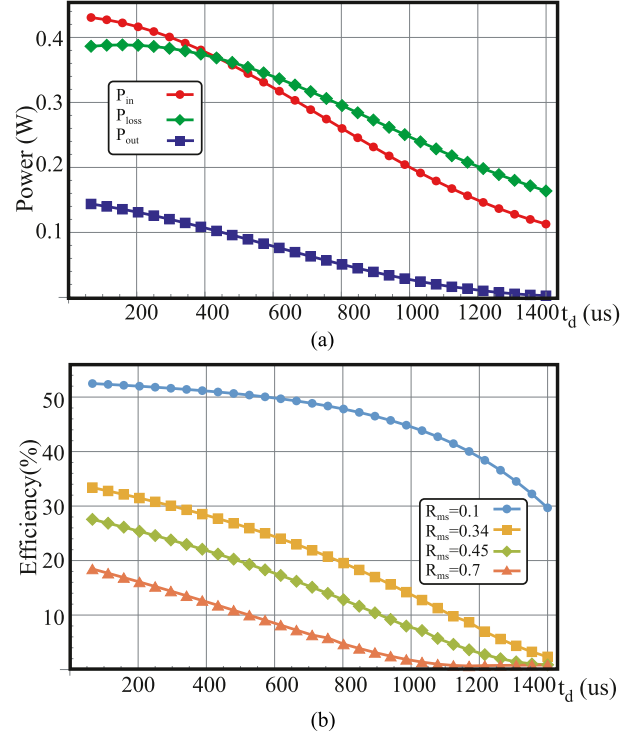


Fig. 8. Theoretically derived power and efficiency of phase delay control. (a) Input power P_{in} , output power P_{out} , and power dissipation P_{loss} when $R_{ms} = 0.34 \Omega$. (b) Efficiency under different R_{ms} .

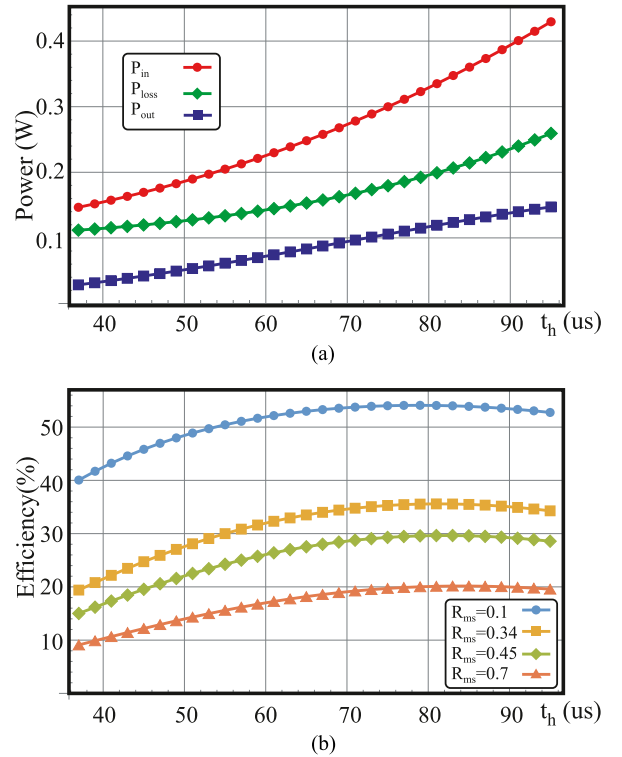


Fig. 9. Theoretically derived power and efficiency of EE interval control. (a) Input power P_{in} , output power P_{out} , and power dissipation P_{loss} when $R_{ms} = 0.34 \Omega$. (b) Efficiency under different R_{ms} .

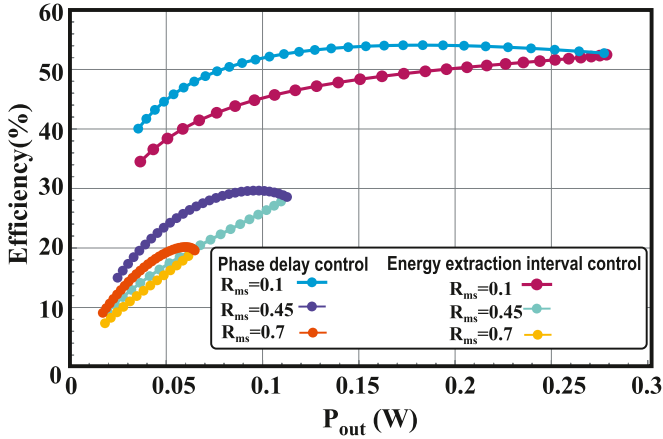


Fig. 10. Theoretically derived efficiency of phase delay control and EE interval control.

G. Comparison and Discussion

The efficiency is the output power at the load side divided by the input power of V_{emf} . So, the output impedance of the EMEH, which is R_m , will contribute to the energy dissipation.

Fig. 10 shows the efficiency of phase delay control and EE interval control versus the output power under different R_{ms} . As the output power increases, both methods show improved efficiency. EE interval control exhibits better efficiency compared to phase delay control over the entire load range. The excess energy in the EMEH will return to the mechanical domain, but some of it will be dissipated in the ESR of the EMEH. For phase delay control, the energy returns to the mechanical domain between t_4 and t_5 in Fig. 5(a), where the current level in the EMEH is higher. So, more energy is dissipated on R_m and R_s in this process. However, for EE interval control, the energy returns to the mechanical domain between t_1 and the first ZCP of i_m in Fig. 5(b), where the current level in the EMEH is lower. This phenomenon is more obvious for EMEHs with a low-quality factor, i.e., higher R_m . While phase delay control does not require as precise timing as EE interval control, its efficiency will be lower. So, if the controller is capable of performing EE interval control at a relatively low energy consumption, it is preferred to use this control method.

IV. CONTROLLER IMPLEMENTATION

The switching frequency of the synchronized technique is much lower than that of direct ac–dc methods, and the switching actions are synchronized with the V_{emf} 's ZCPs. Using a microcontroller unit (MCU) to control SS interface circuits has several advantages. Since the switching action is low frequency and synchronized with the EMEH, the MCU can stay in low-power mode between switching actions. The MCU can utilize its internal comparator to detect ZCPs in low-power mode, thereby achieving low power consumption and eliminating the need for triangle waveform generators or external clock sources.

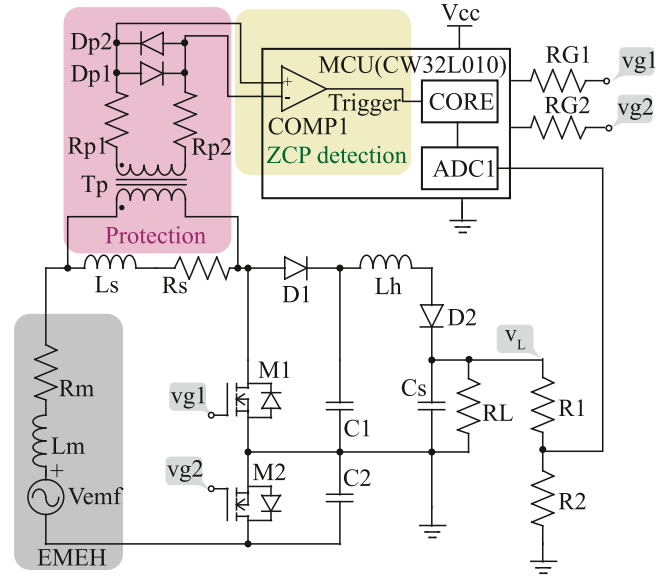


Fig. 11. Overall controller implementation.

Fig. 11 shows the general architecture. We utilize a low-power MCU along with discrete components to control the circuit. The purpose of the MCU is to generate a control signal based on the current information sensed by L_s and the measured output voltage at the load side, while maintaining a relatively low energy consumption.

The control circuit operates without external clock sources, relying on the MCU's high-speed internal clock (HSI) and low-speed internal clock (LSI) for proper operation. The MCU offers different low-power modes, including Sleep mode and DeepSleep mode. In Sleep mode, the core stops, but the HSI remains active, providing high-precision timing while requiring higher power consumption. In DeepSleep mode, only the LSI is active; the power consumption is drastically reduced compared to letting the controller run at full active mode, which needs about 3 mA continuously.

The protection circuit protects the MCU from voltage spikes generated during the CI and EE phases. T_p is a 1:1 signal transformer to filter out the common-mode voltage spikes. R_{p1} , R_{p2} , D_{p1} , and D_{p2} filter out differential voltage spikes. Although the spikes are filtered, the ZCPs of voltage across the sensing inductor can still propagate to the input of the MCU. We only need to detect the ZCPs, as they indicate the current peak of the EMEH. The protection circuit has a negligible impact on the circuit's operation, given that R_{p1} and R_{p2} are sufficiently large, so it can be ignored as if the sensing inductor is directly connected to the comparator inputs.

The MCU detects the ZCPs of the EMEH current with its internal comparator, COMP1, and measures the load voltage v_L through a voltage-dividing network formed by R_1 and R_2 . Since the switching frequency is not high and the sources of M_1 and M_2 are connected to the ground, the MCU can directly drive the MOSFETs through two current-limiting resistors R_{G1} and R_{G2} .

The MCU stays in DeepSleep mode most of the time, as Fig. 12(a) shows. At t_2 , the beginning of the CI phase, the MCU

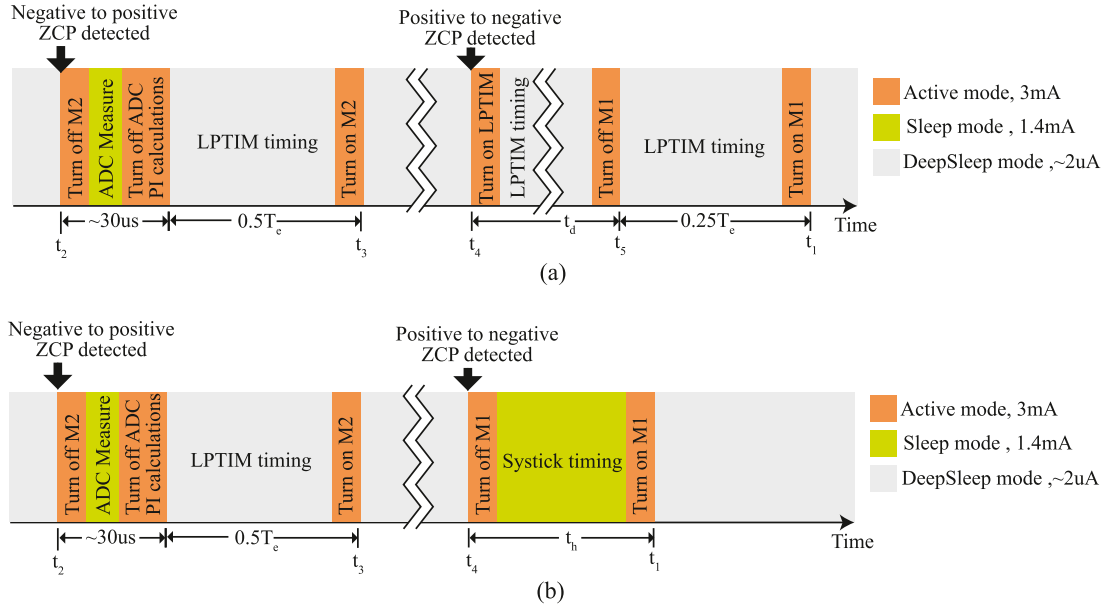


Fig. 12. Operation of the MCU with its associated low-power modes (not to scale). t_1 – t_5 correspond to Fig. 2. $T_e = 2\pi\sqrt{L_{ms}C_1}$ is the resonant cycle of L_{ms} and C_1 . LPTIM is the low-power timer of the MCU. (a) Phase delay control. (b) EE interval control.

wakes up by the COMP1 signal. It performs CI by turning OFF M_2 for a set period. Meanwhile, it measures the output voltage and calculates the control output of the feedback controller. The HSI remains ON during Sleep mode so ADC can operate. After t_3 , the MCU returns to DeepSleep mode. At t_4 , the MCU wakes up again due to the COMP1 signal. It sets its low-power timer (LPTIM) to generate an interrupt after t_d and immediately returns to DeepSleep mode. At t_5 , the MCU wakes up by the LPTIM and performs energy harvesting operations by turning M_1 OFF for a set period.

Fig. 12(b) shows the MCU operation of the EE interval control. The operation is similar to phase delay control. The difference is that the MCU immediately performs energy harvesting at positive-to-negative ZCPs, and the EE interval is controlled by setting the MCU in Sleep mode instead of DeepSleep mode between the turning ON and turning OFF of M_1 to generate a more precise EE interval.

A. Feedback Control

To achieve voltage regulation, feedback control is required, which makes the frequency-domain characteristics, particularly the control-to-output transfer function, of interest. A frequency-domain model can aid in controller design. The operation involves RC resonance, so the current and voltages cannot be linearized to extract a small-signal ac model, as is typically done in analyses of switching dc–dc regulators. Nevertheless, the circuit exhibits several features. The output power is load-independent, the switching frequency is relatively low, and the inductor current waveforms are discontinuous. Those features suggest that the proposed circuit can be regarded as a constant power source delivering power to R_L and C_s , which is similar to a DCM buck–boost converter. Therefore, the dominant-pole approximation can be employed to describe the system behavior [32]. The

control-to-output transfer function can be approximated as

$$G(s) \approx \frac{G_0}{1 + \frac{s}{2\pi f_0}} \quad (31)$$

where G_0 is the dc gain, which can be obtained through theoretical analysis in the previous section or by simulation, and f_p is the pole frequency given by $f_p = 1/(\pi R_L C_s)$ [32].

To validate this approximation, frequency-domain simulations are conducted in conjunction with time-domain waveform analysis. The simulation parameters are: $R_L = 300\Omega$, $C_s = 720\mu\text{F}$, dc value of $V_L = 3.3$ V, $L_m + L_s = 1.63$ mH, $R_m + R_s = 0.52\Omega$, $L_h = 10$ mH, $R_h = 0.88\Omega$. The control signal is between 0 and 1. It is linearly related to t_d or t_h , and its polarity is adjusted so that increasing the control signal increases the output power.

The dc gain is simulated first. The simulated dc gain of phase delay control is 14.7 dBV, and the dc gain of EE interval control is 17.5 dB. Next, a small sinusoidal signal is injected into the control signal. Fig. 13 illustrates the simulated operation waveforms at the pole frequency. For phase-delay control in Fig. 13(a), the gain at $f_p = 1.47$ Hz is 11.3 dB, with a phase shift of -49.3° , representing a 3.5 dB drop from the dc gain. For EE control in Fig. 13(b), the gain and phase at f_p are 13.62 dB and -49.9° , respectively, corresponding to a 3.9 dB drop. These results are consistent with the behavior of a single-pole system.

Fig. 14 shows the frequency-domain response. The curves represent the simulation results, while the straight lines denote the asymptotes of a single-pole system. The response confirms that the system behaves as a single-pole system with a pole at $f_p = 1.47$ Hz and a -20 dB/decade slope beyond that frequency. Additional small delays are introduced by the control circuit and harvesting branch, so the phases drop below -90° at higher frequencies.

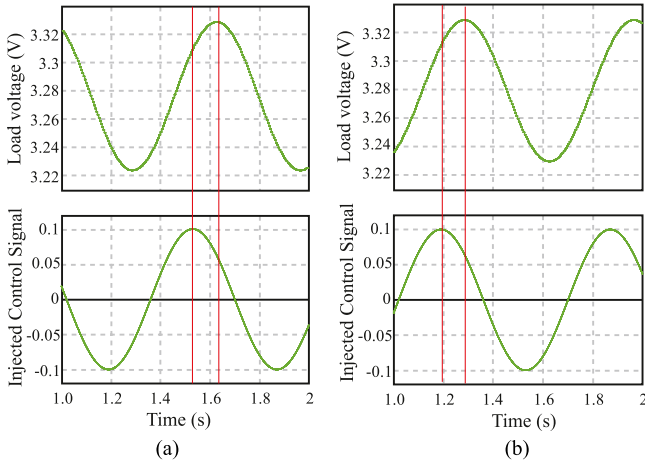


Fig. 13. Simulated waveforms of injected input signal and output voltage, the input signal frequency is 1.47 Hz, and the difference between the red vertical lines is the phase delay. (a) Phase delay control. (b) EE interval control.

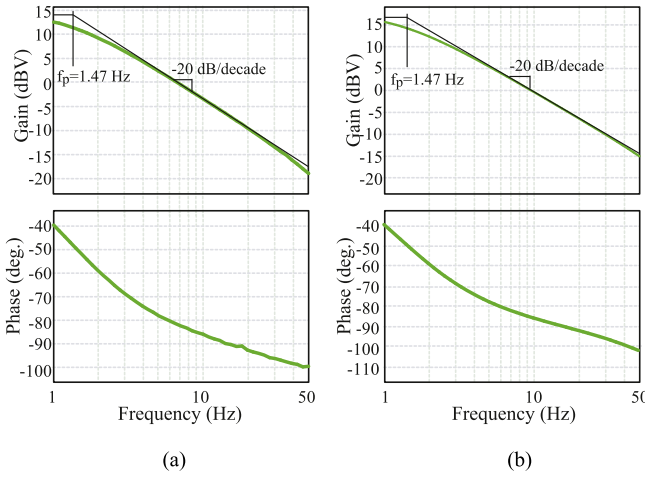


Fig. 14. Simulated frequency-domain response of control signal to output voltage. (a) Phase delay control. (b) EE interval control.

PI controllers are widely used for regulating single-pole systems and have been applied in direct ac–dc converters operating in DCM mode [22], [29]. The Cohen–Coon tuning method can be adopted to select the parameters. By analyzing the output voltage response to small step changes in t_d or t_h during simulation, the PI controller parameters are obtained. The parameters for phase delay control are $K_p = 2.25$ and $T_i = 0.03$; for energy harvesting cycle control, $K_p = 1.56$ and $T_i = 0.03$. Both simulation and subsequent experimental results verify that under these parameters, the PI controller can regulate the output voltage.

So, the PI compensated voltage feedback controller is implemented in the MCU to realize voltage regulation. The MCU compares the measured value of the analog-to-digital converter (ADC) and the target value set by the user and adjusts t_d or t_h accordingly. Since the ADC sampling is synchronized with the switching action, external low-pass filters, such as an RC filter, are unnecessary.

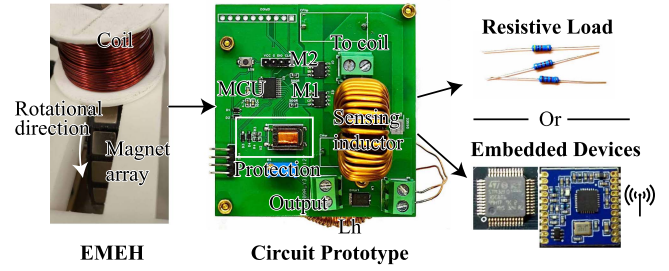


Fig. 15. Experimental setup.

TABLE II
COMPONENT PARAMETERS IN EXPERIMENT

Component	Value / Type
Resonance capacitors C_1, C_2	2.2 μF
Output capacitor C_s	720 μF
EMEH internal inductance L_m	1.41 mH (ESR $R_m = 0.46 \Omega$)
Harvesting inductors L_h	10mH (ESR = 0.88 Ω)
Sensing inductor L_s	0.22mH (ESR = 22 m Ω)
N-channel MOSFET	NCE0110AS ($R_{DS,On} = 20 \text{ m}\Omega$)
Gate Resistors $R_{G1} R_{G2}$	240 Ω
Diodes D1 D2	SB10200 ($V_d = 0.7 \text{ V}$)
Protection transformer T_p	HR228434 (1:1 turn ratio)
$D_{p1} D_{p2}$	1n4148W
$R_{p1} R_{p2}$	51k Ω
$R_1 + R_2$	2M Ω

V. EXPERIMENTS

A. Circuit Prototype and Experimental Setup

A circuit prototype is fabricated. Fig. 15 shows the EMEH and circuit board used in the experiment. The energy harvester is a rotational electromagnetic transducer. A brushless dc motor rotates the magnet array as mechanical excitation. The load can be either pure resistive loads of different values or embedded devices. Table II shows the materials and parameters used in the experiment. The ESRs of the inductors are measured at 211 Hz with an LCR meter (Instek LCR-821). R_m is measured with the prototype circuit, so the resistances of wiring and PCB traces are also included in R_m . R_1 and R_2 are implemented with a 2 M Ω potentiometer. The power dissipation on R_1 and R_2 is around 5 μW at 3.3 V output, which is negligible compared to the output power.

B. Circuit Operation

The first experiment validates the circuit's operation. The EMEH's open circuit voltage amplitude is 1.02 V, and the frequency is 211 Hz. The load resistance $R_L = 325 \Omega$. The output voltage is set to 3.3 V. Fig. 16(a) shows the measured EMEH current and output voltage when the control method is EE interval control. Fig. 16(b) shows the measured waveforms for the phase delay control. The measured waveforms agree with conceptual ones in Figs. 2 and 4, indicating that the system operates as intended.

The steady-state output power of the proposed system is evaluated under different loads. The output voltage V_L is set to 3.3 V, and the load resistance R_L varies from 130 to 745 Ω .

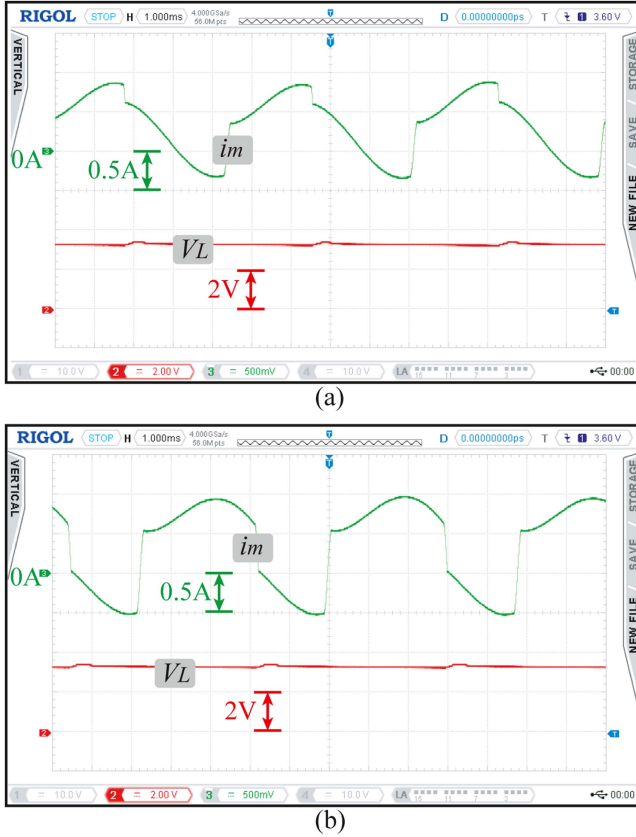


Fig. 16. Experimental waveform of (a) EE interval control and (b) phase delay control.

The EE intervals t_h at different load resistances are measured by observing the voltage waveform on the gate of M_1 . The theoretical output power for different EE intervals is calculated based on (18) and the theoretical analysis of the harvest branch in [28], while the actual output power is given by $P_{out} = V_L^2/R_L$. Fig. 17(a) shows the relationship between the EE interval and output power theoretically and experimentally. The same experiment is repeated for phase delay control, and Fig. 17(b) shows the evaluation results for phase delay control. Overall, the theoretical derivations and experimental data agree well.

The power and loss distribution is theoretically derived based on the current values of resistors and diodes derived in Section III. The theoretically derived results are compared to simulation results. Table III shows the theoretically derived and simulated power distribution. The ESR of the EM transducer causes most of the energy dissipation. Most of this is dissipated during the SC phase. While the dispersed energy is significant, more energy can be extracted from the harvester compared to other harvesting schemes; therefore, the overall energy output remains larger. The experimentally measured, simulated, and theoretically derived outputs are in close agreement. The gate-driving losses of MOSFETs are negligible compared to other losses. The EMEH output resistance R_m accounts for most of the power loss. Phase delay control is more straightforward to implement because its timing requirement is not as strict as EE interval control. However, for the same output power, phase delay control dissipates more power due to the reactive power

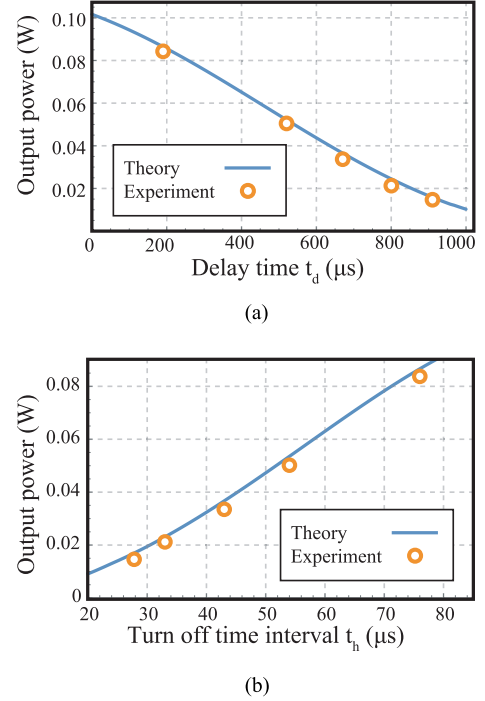


Fig. 17. Theoretically derived and experimentally measured output power at the load side. (a) EE interval control. (b) Phase delay control.

TABLE III
POWER DISTRIBUTION AND LOSS BREAKDOWN AT 130 Ω LOAD

Energy extraction interval control		
Power	Theory	Simulation
Output Power	83.6 mW	83.4 mW
R_m	141 mW	140 mW
R_s and $R_{DS,On}$	21 mW	21 mW
D_1	17.9 mW	17.6 mW
D_2	17.7 mW	17.6 mW
R_h	4.62 mW	4.34 mW
Phase delay control		
Output Power	86.9 mW	83.5 mW
R_m	205 mW	203 mW
R_s and $R_{DS,On}$	30 mW	30 mW
D_1	18.6 mW	17.7 mW
D_2	18.4 mW	17.7 mW
R_h	4.93 mW	4.32 mW

* Simulation Condition: Source amplitude is 1.0 V @ 211 Hz, load Voltage is 3.3 V, load Resistance is 130 Ω.

induced in the transducer, so EE interval control is preferred in terms of efficiency, as discussed in Section III-G. The simulation results and theoretical derivations are in good agreement.

A bench power supply powers the control circuit. The average current consumption of the MCU is measured through a multimeter to evaluate the power consumption of the control part. For phase delay control, the power consumption of the control circuit is 264 μ W at 3.3 V. As for EE interval control, the power is 297 μ W. The ADC measurements and feedback controller calculations account for most of the power consumption of the MCU. In the experiment, if the control part performs switching actions only, then the measured power at the VCC terminal is only 75 μ W, including gate driving, approximately 33 μ W in theory.

The power consumption of the control circuit increases or decreases with the source frequency. Because the operation of the MCU is synchronized with the source, this increase or decrease is proportional to the source frequency. In addition, for EE interval control, the power consumption varies by as much as $15 \mu\text{W}$, depending on load conditions at 211 Hz. This variation is because the time length of Sleep mode during EE intervals changes with load power. This variation is slight compared to the system's output power. Keeping the MCU in low-power modes most of the time has reduced the power consumption of the MCU from 9.9 mW to less than 0.3 mW.

The control circuit requires only a single power supply, and its low power consumption makes self-powered operation feasible. For verification, the control circuit's power supply, VCC, is directly connected to the output of the energy harvesting circuit, so $V_{CC} = V_L$. The system is cold-started by precharging C_s with an external power supply. After a cold start, the external power supply can be removed, and the system can operate continuously in experiments. In future designs, with the help of additional cold-start circuits, such as those in [6], [15], and [21], the system can achieve self-startup. The MCU's power consumption is less than 1% of the output power, so it has a negligible impact on the output.

C. Load Transients, Source Transients, and Powering IoT Devices

The proposed circuit's operation waveforms are recorded when source and load conditions vary. In Fig. 18(a) and (b), the load condition varies. The load is an embedded system comprising an STM32F030 microcontroller and a PAN3029 wireless transceiver module, which together are capable of integrated circuit long range (LoRa) packet transmission. It is programmed to transmit a packet to a host device and receive a packet from the host device. As Fig. 18 shows, the load current undergoes several step changes during transmission and reception.

The output of the proposed circuit is directly connected to the power pin of the embedded system load without any additional voltage regulator. The embedded system load consumes 18 mA during packet transmission, 8 mA during packet reception, and $300 \mu\text{A}$ in the idle state. The load voltage overshoot and undershoot during the load current transient are lower than 0.2 V, and the voltage ripple during transmission is approximately 0.15 V for both cases. The overshoot and undershoot are slightly larger for phase delay control since its response is a bit slower. The embedded system load has successfully transmitted and received a LoRa packet, indicating that the interface circuit can power the embedded system in IoT applications.

In Fig. 18(c) and (d), the source condition varies. The load is a 325Ω resistor, and the source voltage is adjusted by changing the position of the energy harvester's coil. The source voltage amplitude changes as the coil moves back and forth, and the harvester current i_m fluctuates accordingly. The output voltage remains steady at 3.3 V during this process. The proposed power control method, combined with a PI-compensated feedback controller, can effectively maintain the load voltage under varying load and source conditions.

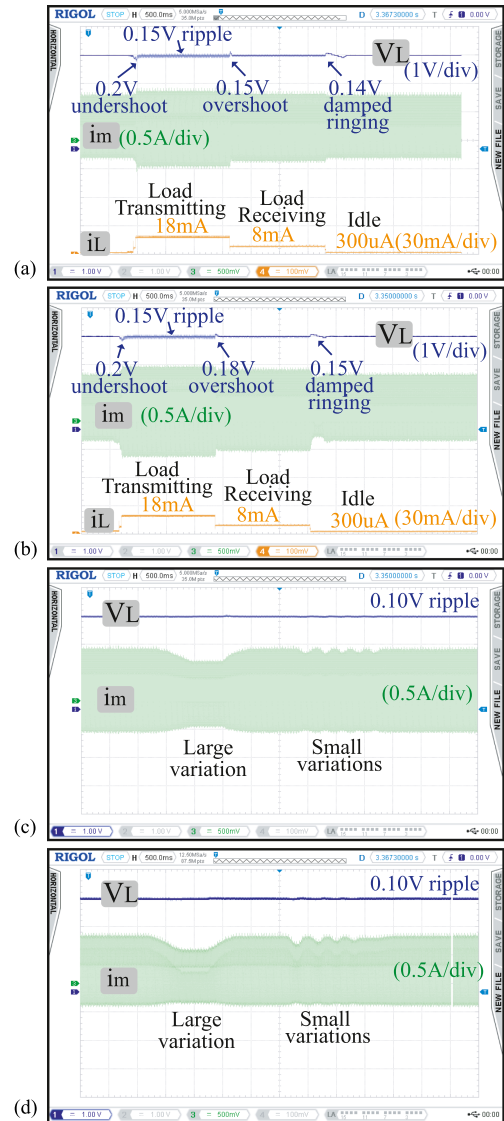


Fig. 18. Measured waveform of the proposed control method during source and load transients. (a) Load transient response of the EE interval control. (b) Load transient response of phase delay control. (c) Source transient response of the phase delay control. (d) Source transient response of the EE interval control.

D. Performance Comparison With SSEE, Direct AC–DC Boost Topology, and Two-Stage Topology

Another circuit prototype for the SSEE harvesting scheme in [25] and the direct ac–dc conversion scheme is fabricated using the same PCB board and components for comparison. By removing C_2 and adding another diode D_{SSEE} (on the right edge of the PCB in Fig. 15), the circuit operates like an SSEE circuit. In addition, if L_h is short-circuited and the control signal is changed to a high-frequency PWM signal, then the circuit operates as a direct ac–dc boost converter. The output voltage control of the SSEE circuit is achieved by delaying the EE operation, similar to Fig. 2.

The load of this experiment is the embedded system from Section V-C. The transmitting power is set to 11 dBm, the embedded system load consumes 37 mA during packet transmission, and the source voltage amplitude is 0.85 V.

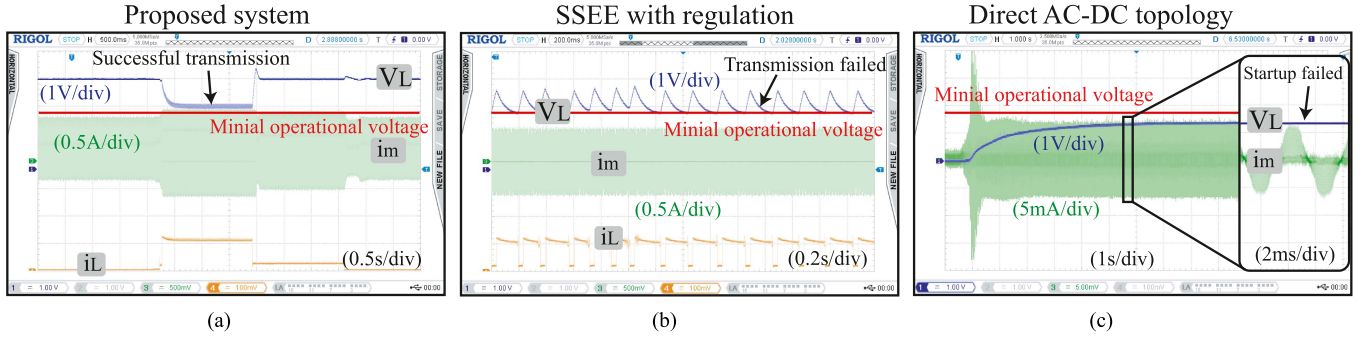


Fig. 19. Measured waveform of (a) Proposed system, (b) SSEE harvesting scheme, and (c) direct AC–DC boost harvesting scheme. The red line is the minimal voltage required by the LoRa transmission module to operate.

The three harvesting schemes are deployed to power the embedded system load. Fig. 19 shows the recorded waveform in the experiment. When the embedded system load is powered by the proposed system, as in Fig. 19(a), the output voltage dropped to 2.3 V, but since this voltage is still within the operational voltage range of the embedded system, LoRa transmission is still functional, so the embedded system successfully transmitted a LoRa packet. For the SSEE harvesting scheme, the embedded system can perform system initialization, but fails during transmission since the maximum available power of the SSEE harvesting scheme is insufficient. In the case of direct ac–dc boost harvesting, the leakage from the embedded system prevented the output voltage from rising above the minimum required voltage, causing the embedded system load to fail to start.

Another two-stage topology is fabricated to evaluate the performance of the proposed single-stage voltage regulation solution with a two-stage voltage regulation solution. The two-stage topology consists of a normal SCIEE circuit in series with a commercial dc–dc regulator MT2492; the energy buffer capacitance at the output of the SCIEE circuit, which is also the input of the MT2492 dc–dc regulator, is 720 μ F.

The different harvesting schemes' maximum supported load current is measured by measuring the maximum output current at a 3.3 V output voltage. The maximum current of the direct ac–dc topology is measured to be 0.2 mA. The SSEE circuit's maximum output current is 27.31 mA. The two-stage topology's maximum output is 27.25 mA, and the proposed single-stage solution can output 29.47 mA. The maximum output current of the two-stage topology is 92.5% of that of the single-stage topology, consistent with the datasheet specifications of the commercial dc–dc regulator used in the second stage.

VI. DISCUSSIONS

A. Comparison of Two-Stage Topology and the Proposed Single-Stage Power Control Solution

V_{emf} is an internal equivalent voltage source within the EMEH, making end-to-end efficiency difficult to measure directly in experiments. Some works would measure the end-to-end efficiency at the output of the EMEH [22], but in SS circuits, the EMEH's output impedances L_m and R_m participate in the

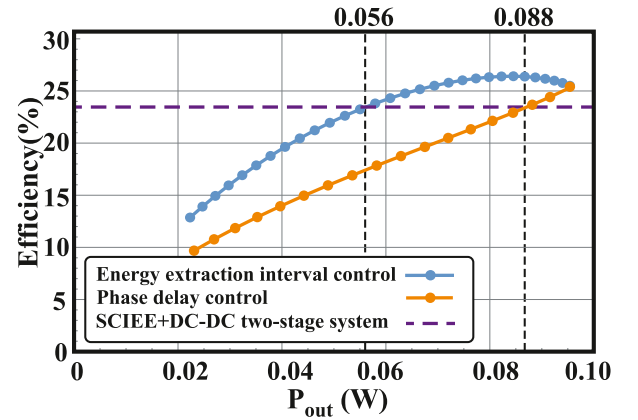


Fig. 20. Theoretically derived efficiency of EE interval control, phase delay control, and the two-stage topology.

circuit operation, so the impact on the performance is not negligible. Therefore, this section discusses efficiency and energy transfer performance based on simulation results and theoretical analysis.

For a two-stage energy harvesting system consisting of a normal SCIEE circuit in series with an energy buffer and a commercial dc–dc regulator, the input power and output power do not match, so some control method is still required to keep the system from overvoltage, for example, letting the SCIEE circuit operate intermittently with a certain duty cycle instead of continuously. Under ideal conditions, the efficiency of the first stage of this two-stage topology can still be η_{sciee} when operating intermittently, where η_{sciee} is the efficiency of the SCIEE circuit during operation. So, the efficiency of a two-stage energy harvesting system for a given load P_{out} would be

$$\eta_{two_stage} = \eta_{sciee} \cdot \eta_{dc-dc} \quad (32)$$

over the entire load range, where η_{dc-dc} is the efficiency of the commercial dc–dc regulator. On the other hand, the efficiency of the proposed single-stage topology can be calculated with the theoretical analysis in Section III-F. Fig. 20 shows the theoretically derived efficiency of the single-stage system and that of the two-stage topology when $\eta_{dc-dc} = 0.92$. The parameters are the same as those in table II.

TABLE IV
COMPARISON OF DIFFERENT ENERGY HARVESTING SCHEMES UNDER THE SAME MECHANICAL EXCITATION

Harvesting scheme	Direct AC-DC topology [22]	SP-SMFE [15]	SSEE [25]	SCIEE [28]	SCIEE+DC-DC	This work
Gate driving complexity	medium	low	high	low	low	low
Voltage regulation	yes	no	no	no	yes	yes
Polarity detection	not required	required	required	required	required	required
Inductor count	1	1	3	2	3	2
Switching frequency ^(a)	50 kHz	422 Hz	422 Hz	422 Hz	422 Hz + 600 kHz	422 Hz
Voltage ripple ^(b)	5.4 μ V	-	0.64 mV ^(d)	-	0.45 μ V	1.28 mV
Maximum output power ^(c)	0.66 mW	-	90.12 mW	97.25 mW	89.93 mW	97.25 mW
Supported load current range ^(c)	0-0.20 mA	-	0-27.31 mA ^(d)	-	0-27.25 mA	0-29.47 mA
Controller	DSP	analog circuit	analog circuit	microcontroller	microcontroller	microcontroller
Controller power consumption	-	-	5 mW	-	-	0.3 mW
Self-powered	yes	yes	yes	no	no	yes
Self startup without percharging	no	yes	no	no	no	no

^(a) The switching frequency used in the comparison experiments

^(b) Derived at 0.2 mA load current and 720 μ F load capacitor

^(c) Load voltage is 3.3 V

^(d) When adopted with the control method in this paper

A two-stage topology demonstrates better efficiency for light-load conditions at the cost of extra components for the second stage. For heavier loads, the proposed single-stage topology can outperform the SCIEE+dc-dc configuration. In the prototype, the efficiency of EE interval control is higher than that of the two-stage topology when the output power is higher than 56 mW, which is around 41.3% of the supported output power range. On the other hand, the output power needs to be higher than 88 mW for the phase delay control's efficiency to be higher. The analytical results in Fig. 10 suggest the proposed solution would have better efficiency for a wider load range for smaller R_{ms} .

Although the proposed single-stage system introduces some efficiency loss under light-load conditions, it improves performance under heavy-load scenarios and offers higher peak power. In typical IoT applications, energy is relatively abundant when the system remains in sleep mode, so lower power conversion efficiency is tolerable. During brief periods of wireless communication, the system experiences a heavy load, during which reliable operation requires sufficient output power, so the proposed design is valuable for such applications.

Some performance metrics, such as voltage ripple, undershoot, overshoot, and response time, are strongly influenced by factors, including the selected components, load conditions, and selection of the dc-dc regulator integrated circuit (IC). In general, due to the lower switching frequency of the single-stage topology compared to that of commercial dc-dc regulators, it would exhibit larger voltage ripple and higher undershoot or overshoot for the same output capacitance. However, the effect of those drawbacks can be reduced through the appropriate selection of output capacitance and careful controller loop design.

B. Comparison of Different Energy Harvesting Solutions

Table IV compares different harvesting schemes. The direct ac-dc boost topology is capable of voltage regulation. Still, its energy harvesting capability is limited when the output impedance of the EMEH is large and mainly inductive. SMFE, SSEE, and SCIEE circuits are based on the SS technique and can harvest more energy under those conditions at the cost of additional transducer current polarity detection. The switching frequency is lower, so a larger output filter capacitor and larger

inductance are required. However, the low switching frequency has also made control easier and more power-efficient. The proposed system's microcontroller consumes only 0.3 mW, which is lower than the 5 mW consumption of the analog controller in the SSEE circuit [25]. The low-power feature of the controller also enables self-powered operation at the steady state, allowing the controller to directly draw power from the load, provided the load capacitor is precharged for the system to start up. A two-stage topology, consisting of an SCIEE circuit in series with a commercial dc-dc regulator, can achieve better efficiency at light loads. Still, since another stage introduces additional power loss, its maximum supported load current is not as high as that of a single-stage solution. Two-stage topologies also require more components. Combined with the power control method proposed in this article, SS interface circuits can achieve single-stage voltage regulation and a relatively larger supported load range, enabling applications in IoT systems that require relatively high peak output power and regulated voltage output. By adopting the SS technique and implementing single-stage voltage regulation, the proposed system achieves higher output power and improved efficiency under heavy-load conditions compared to direct ac-dc rectifiers and the two-stage topology.

VII. CONCLUSION

SS interface circuits have been reported to enhance the output power of EMEHs. However, existing SS circuits for EMEHs cannot control their output. This article proposes an SS interface circuit implemented with two power control methods, adding a control degree of freedom to the SS circuits.

This system enables applications in IoT systems that require a regulated voltage output. It controls power by changing the phase of the control signal or changing the time duration of the energy harvesting phase, achieving single-stage voltage regulation. A theoretical analysis of the relationship between control signals and EMEH power output has been conducted. The efficiency and loss of the two control methods have also been theoretically analyzed and compared, showing that changing the time duration of the energy harvesting phase achieves better efficiency for the same loading condition. Theoretical prediction and simulation results agree well.

The implementation of a controller using an MCU is elaborated. A circuit prototype has been fabricated to validate the proposed circuit. The circuit operates as designed. The output power at different control signals of the circuit prototype has been measured. The measured results agree with theoretical derivations. The MCU's power consumption is also measured to be less than 300 μW , about 3% compared to continuous operation, suggesting that utilizing low-power modes for low-switching-frequency applications has benefits. Experiments have also validated the feasibility and effectiveness of the proposed control scheme under different load and source conditions.

Experiments evaluated the performance of the direct ac–dc topology, the SSEE circuit implemented with the proposed power control method, an SCIEE circuit in series with a commercial dc–dc regulator, and an SCIEE circuit implemented with the proposed control method. The proposed system showed the widest supported load range.

Further analysis shows that compared to using a commercial dc–dc regulator for voltage regulation, using the single-stage topology with the proposed power control method exhibits a wider supported load range, fewer components, and better efficiency for output power larger than 56 mW.

In the field test for transmitting a LoRa packet under the same mechanical excitation, the proposed circuit's performance was compared to two other harvesting schemes: synchronized switch energy extraction (SSEE) and direct ac–dc conversion. The SCIEE circuit can support successful transmission when the other two schemes fail due to insufficient power, demonstrating a wider range of supported loads.

REFERENCES

- [1] S. F. Nabavi, A. Farshidianfar, and A. Afsharfard, "Novel piezoelectric-based ocean wave energy harvesting from offshore buoys," *Appl. Ocean Res.*, vol. 76, pp. 174–183, 2018.
- [2] M. A. Abdelkareem et al., "Vibration energy harvesting in automotive suspension system: A detailed review," *Appl. Energy*, vol. 229, pp. 672–699, 2018.
- [3] X. Li et al., "ViPSN: A vibration-powered IoT platform," *IEEE Internet Things J.*, vol. 8, no. 3, pp. 1728–1739, Feb. 2021.
- [4] A. Ali, H. Shaukat, S. Bibi, W. A. Altabay, M. Noori, and S. A. Kouritem, "Recent progress in energy harvesting systems for wearable technology," *Energy Strategy Rev.*, vol. 49, 2023, Art. no. 101124.
- [5] W. Zeng et al., "A self-powered P–SSHI and boost hybrid interface circuit for multi-PZTs and low voltage electromagnetic energy extraction," *Microelectronics J.*, vol. 135, 2023, Art. no. 105745.
- [6] R. Dayal, S. Dwari, and L. Parsa, "A new design for vibration-based electromagnetic energy harvesting systems using coil inductance of microgenerator," *IEEE Trans. Ind. Appl.*, vol. 47, no. 2, pp. 820–830, Mar./Apr. 2011.
- [7] E. Arroyo and A. Badel, "Electromagnetic vibration energy harvesting device optimization by synchronous energy extraction," *Sens. Actuators A: Phys.*, vol. 171, no. 2, pp. 266–273, 2011.
- [8] S. Sun, X. Dai, K. Wang, X. Xiang, G. Ding, and X. Zhao, "Nonlinear electromagnetic vibration energy harvester with closed magnetic circuit," *IEEE Magn. Lett.*, vol. 9, 2018, Art. no. 6102604.
- [9] X. Dai et al., "A hybrid energy harvesting system for self-powered applications in shared bicycles," *Sustain. Energy Technol. Assessments*, vol. 51, 2022, Art. no. 101891.
- [10] H. Zhang, S. Zhou, H. Xu, and S. Zhou, "A high-performance rotational electromagnetic energy harvester based on magnetic plucking: Design, simulation, and experiment," *Mech. Syst. Signal Process.*, vol. 204, 2023, Art. no. 110778.
- [11] H. Fu et al., "Rotational energy harvesting for self-powered sensing," *Joule*, vol. 5, no. 5, pp. 1074–1118, 2021.
- [12] T. Wang, H. Lv, and X. Wang, "Development of an electromagnetic energy harvester for ultra-low frequency pitch vibration of unmanned marine devices," *Appl. Energy*, vol. 353, 2024, Art. no. 122072.
- [13] H. Cao et al., "An electromagnetic energy harvester for applications in a high-speed rail pavement system," *Int. J. Mech. Sci.*, vol. 243, 2023, Art. no. 108018.
- [14] T. Zhang et al., "An electromagnetic vibration energy harvesting system based on series coupling input mechanism for freight railroads," *Appl. Energy*, vol. 353, 2024, Art. no. 122047.
- [15] S. Jia, C. Zeng, G. Shi, C. Hong, J. Han, and Y. Xia, "A self-powered synchronous magnetic flux extraction interface for electromagnetic energy harvesting," *Microelectronics J.*, vol. 140, 2023, Art. no. 105943.
- [16] X. Cao, W.-J. Chiang, Y.-C. King, and Y.-K. Lee, "Electromagnetic energy harvesting circuit with feedforward and feedback DC–DC PWM boost converter for vibration power generator system," *IEEE Trans. Power Electron.*, vol. 22, no. 2, pp. 679–685, Mar. 2007.
- [17] A. Tabesh and L. G. Frechette, "A low-power stand-alone adaptive circuit for harvesting energy from a piezoelectric micropower generator," *IEEE Trans. Ind. Electron.*, vol. 57, no. 3, pp. 840–849, Mar. 2010.
- [18] S. Guo and H. Lee, "An efficiency-enhanced CMOS rectifier with unbalanced-biased comparators for transcutaneous-powered high-current implants," *IEEE J. Solid-State Circuits*, vol. 44, no. 6, pp. 1796–1804, Jun. 2009.
- [19] A. Rahimi, O. Zorlu, A. Muhtaroglu, and H. Kulah, "Fully self-powered electromagnetic energy harvesting system with highly efficient dual rail output," *IEEE Sensors J.*, vol. 12, no. 6, pp. 2287–2298, Jun. 2012.
- [20] M. Shousha, D. Dinulovic, M. Haug, T. Petrovic, and A. Mahgoub, "A power management system for electromagnetic energy harvesters in battery/batteryless applications," *IEEE Trans. Emerg. Sel. Topics Power Electron.*, vol. 8, no. 4, pp. 3644–3657, Dec. 2020.
- [21] R. Dayal, S. Dwari, and L. Parsa, "Design and implementation of a direct AC–DC boost converter for low-voltage energy harvesting," *IEEE Trans. Ind. Electron.*, vol. 58, no. 6, pp. 2387–2396, Jun. 2011.
- [22] L. Wang, H. Wang, M. Fu, Z. Xie, and J. Liang, "Three-port power electronic interface with decoupled voltage regulation and MPPT in electromagnetic energy harvesting systems," *IEEE Trans. Ind. Appl.*, vol. 58, no. 2, pp. 2144–2154, Mar./Apr. 2022.
- [23] D. Guyomar, A. Badel, E. Lefeuvre, and C. Richard, "Toward energy harvesting using active materials and conversion improvement by nonlinear processing," *IEEE Trans. Ultrason., Ferroelectr., Freq. Control*, vol. 52, no. 4, pp. 584–595, Apr. 2005.
- [24] E. Lefeuvre, A. Badel, C. Richard, and D. Guyomar, "Piezoelectric energy harvesting device optimization by synchronous charge extraction," *J. Intell. Mater. Syst. Struct.*, vol. 16, pp. 865–876, 2005.
- [25] Z. Xie, L. Teng, H. Wang, Y. Liu, M. Fu, and J. Liang, "A self-powered synchronous switch energy extraction circuit for electromagnetic energy harvesting enhancement," *IEEE Trans. Power Electron.*, vol. 38, no. 8, pp. 9972–9982, Aug. 2023.
- [26] S. Jia et al., "A self-powered interface circuit for simultaneous piezoelectric and electromagnetic energy extraction," *IEEE Trans. Power Electron.*, vol. 38, no. 9, pp. 10640–10650, Sep. 2023.
- [27] G. Lombardi and M. Lallart, "Synchronous electric charge and induced current extraction (SECICE): A unified nonlinear technique combining piezoelectric and electromagnetic harvesting," *Smart Mater. Struct.*, vol. 30, no. 2, 2021, Art. no. 025029.
- [28] J. Qiu, H. Wang, Y. Liu, M. Fu, and J. Liang, "A synchronous current inversion and energy extraction circuit for electromagnetic energy harvesting enhancement," *IEEE Trans. Circuits Syst. I: Reg. Papers*, vol. 71, no. 12, pp. 5471–5481, Dec. 2024.
- [29] L. Yu, H. Wang, and A. Khaligh, "A discontinuous conduction mode single-stage step-up rectifier for low-voltage energy harvesting applications," *IEEE Trans. Power Electron.*, vol. 32, no. 8, pp. 6161–6169, Aug. 2017.
- [30] G. Buja and M. Kazmierkowski, "Direct torque control of PWM inverter-fed AC motors - A survey," *IEEE Trans. Ind. Electron.*, vol. 51, no. 4, pp. 744–757, Aug. 2004.
- [31] Z. Xie, L. Teng, Y. Yin, and J. Liang, "Synchronous switch energy extraction circuit for motor regenerative braking enhancement," *IEEE Trans. Circuits Syst. II: Exp. Briefs*, vol. 70, no. 5, pp. 1779–1783, May 2023.
- [32] R. W. Erickson and D. Maksimovic, *Fundamentals of Power Electronics*. Berlin, Germany: Springer, 2007.